ARTICLE OPEN

Path toward manufacturable superconducting qubits with relaxation times exceeding 0.1 ms

J. Verjauw[1,2], R. Acharya[1,3], J. Van Damme[1,3], Ts. Ivanov[1], D. Perez Lozano[1,3], F. A. Mohiyaddin[1], D. Wan[1], J. Jussot[1], A. M. Vadiraj[1], M. Mongillo[1], M. Heyns[1,2], I. Radu[1], B. Govoreanu[1] and A. Potočnik[1] ✉

As the superconducting qubit platform matures towards ever-larger scales in the race towards a practical quantum computer, limitations due to qubit inhomogeneity through lack of process control become apparent. To benefit from the advanced process control in industry-scale CMOS fabrication facilities, different processing methods will be required. In particular, the double-angle evaporation and lift-off techniques used for current, state-of-the-art superconducting qubits are generally incompatible with modern-day manufacturable processes. Here, we demonstrate a fully CMOS compatible qubit fabrication method, and show results from overlap Josephson junction devices with long coherence and relaxation times, on par with the state-of-the-art. We experimentally verify that Argon milling—the critical step during junction fabrication—and a subtractive-etch process nevertheless result in qubits with average qubit energy relaxation times T_1 reaching 70 μs, with maximum values exceeding 100 μs. Furthermore, we show that our results are still limited by surface losses and not, crucially, by junction losses. The presented fabrication process, therefore, heralds an important milestone towards a manufacturable 300 mm CMOS process for high-coherence superconducting qubits and has the potential to advance the scaling of superconducting device architectures.

npj Quantum Information (2022)8:93 ; https://doi.org/10.1038/s41534-022-00600-9

INTRODUCTION

Superconducting circuits have emerged as a leading candidate for realizing a scalable quantum computing platform. The improvements in qubit coherence times[1] and gate fidelities[2–5] enabled the demonstration of quantum simulators[6,7], small-scale quantum algorithms[8,9], and even the elusive demonstration of quantum supremacy[10,11]. State-of-the-art coherence times routinely reach 50 μs, with specific cases exceeding 100 μs[12–15]. These have been exclusively fabricated using aluminum (Al) double-angle evaporation and lift-off techniques on sapphire or high-resistivity silicon (Si) substrates. Double-angle evaporated junctions enabled the fabrication of Noisy Intermediate Scale Quantum (NISQ) processors with an intermediate scale number of qubits[10,11], only recently exceeding 100[16]. To further advance the technological state-of-the-art, the design and device fabrication inevitably become increasingly complex[17,18]. This imposes tighter constraints on the design parameters of qubits, readout resonators, on-chip filters[19,20], and tunable couplers[21,22]. To facilitate this upscaling, versatile, reliable, and reproducible fabrication processes are needed.

The large-scale implementation of superconducting qubits is inherently hindered by the variability in Josephson energy of the double-angle evaporated junctions[23,24]. This is primarily a consequence of the variability in fabricated junction area, which results from the angle dependence across the wafer during metal deposition[24–26]. Another limitation is that polymer masks that are typically used during processing restrict the thermal budget. This further limits the choice of superconductor, limiting the potential optimization space for qubit improvement[27,28]. Furthermore, the fabrication itself requires dedicated evaporation tools with tilt capability. Double-angle evaporation with a required lift-off step introduces resist contaminations[29] and reduces reproducibility in larger diameter wafers[25]. This fabrication technique is therefore considered incompatible with advanced complementary metal-oxide semiconductor (CMOS) manufacturing, where large-scale integration of devices is instead generally based on subtractive etch, sputtering deposition, and advanced optical lithography[30]. To overcome these limitations, alternative junction fabrication techniques are being actively investigated.

Several alternatives to double-angle evaporated junctions exist, including finMET[31], trilayer[30,32], and overlap[33–37] Josephson junctions. These are compatible with manufacturable CMOS processes. The advantages of overlap junctions compared to other alternatives are the reduced structural complexity and, therefore, a smaller number of fabrication steps. This reduces the processing-induced sources of loss and parameter variability. Recent work has shown promising overlap junction qubit performance, with energy relaxation T_1 times up to 80 μs[33,36,38]. However, these qubits were still created using a CMOS-incompatible lift-off process. Qubits with state-of-the-art coherence times, fabricated with a fully manufacturable CMOS process, i.e., without the use of lift-off techniques, sapphire, or high resistivity (above ~10 kΩ·cm) Si substrates, are yet to be demonstrated.

Overlap junctions have two electrodes that are defined in two patterning cycles, with a vacuum break in between which results in the uncontrolled growth of native metal oxide. After the first cycle, the native oxide needs to be removed by in-situ argon (Ar) milling to enable controlled subsequent junction oxidation. This step is critical since Ar milling has been linked to superconducting device performance degradation[15,39,40]. Strong Ar milling can lead to amorphized Si[41] and sapphire[29] substrate layers, which were found to limit resonator quality factors and qubit coherence times. The milling has also been reported to introduce additional loss at metal–metal interfaces[15]. This indicates that the Ar milling could compromise the junction's integrity and composition. However,

[1]Imec, Kapeldreef 75, 3001 Leuven, Belgium. [2]Department of Materials Engineering (MTM), KU Leuven, 3000 Leuven, Belgium. [3]Department of Electrical Engineering (ESAT), KU Leuven, 3000 Leuven, Belgium. ✉email: anton.potocnik@imec.be

the impact of Ar milling on the junction performance is still unexplored, and at present, it is unknown if it inherently limits the overlap junction qubit lifetimes.

In our work, we perform an in-depth characterization of Al overlap junctions, fabricated with wet and dry subtractive-etch processes. Intrinsic Si substrate coupons with 3 kΩ·cm (3k) and 20 kΩ·cm (20k) specific resistivity are used from 300 and 100 mm wafers, respectively. Results for fixed frequency transmon qubits with overlap junctions show time-averaged energy relaxation T_1 times of 50–70 μs, with individual measurements surpassing 100 μs, and average Pauli gate fidelity of 99.94%. By comparing quality factors ($Q = 2\pi T_1 f$) of qubits with different capacitor geometries, we find that the total loss ($1/Q$) scales with the metal–air surface oxide participation ratio, suggesting that the qubits are limited by the surface losses residing at the capacitor pads instead of the junction. The dominant loss likely originates from the subtractive-etch-specific sidewall residues and native surface oxides. Our study reveals that the overlap junctions do not limit the T_1 coherence time up to at least 131 μs for qubits at 3 GHz.

RESULTS

Overlap junction fabrication and room-temperature characterization

The process used to fabricate transmon qubits with overlap Josephson junctions is based on previously published work[33,38] and is described in detail in the Methods section and Supplementary Fig. 1. A 70 nm Al film is sputtered on a hydrofluoric (HF) acid-cleaned, high-resistivity Si substrate. Qubit capacitor pads, readout resonators, ground plane, and overlap junction bottom electrode (BE) are defined simultaneously using either a dry or wet subtractive etch. Fabricating these structures in a single layer minimizes the number of interfaces. Next, native oxides from the entire surface including BE are removed using an optimized Ar milling step inside the deposition tool. This step impacts the BE–air, Si–air, and junction interfaces. Following the native oxide removal, a controlled dynamic oxidation is performed to create the junction barrier. Next, a 50 nm thick top Al layer is deposited. In the final step, the top electrode (TE) is patterned with a subtractive dry etch. The targeted overlap junction areas are in the range of 0.03–0.07 μm^2. In addition to the overlap junction, the TE forms a large stray junction (~10 × 20 μm) used as galvanic contact to the qubit's capacitor pad (Fig. 1a: blue interface). A scanning tunneling electron microscope (STEM) image of a fabricated overlap junction is shown in Fig. 1b. Devices fabricated with the described process exhibit record-high qubit energy relaxation times for overlap Josephson junction qubits, exceeding 100 μs (Fig. 1c). Furthermore, randomized benchmarking[42] yields average single qubit gate fidelities of $F_{1q} = (99.940 \pm 0.003)\%$, which are very close to the coherence limit of $F_{1q,inc} = 99.96\%$ (see Methods section and Fig. 1d). The uncertainty on the values represents the standard deviation (SD) on the fit.

We perform both wet and dry subtractive etching to define the BE. Wet etch processes are selective to Si and leave the substrate's top-surface intact. It can be argued that they yield better qubit coherence times[14] and resonator quality factors[43] compared to dry-etched devices, as the latter can be affected by an increase in Si substrate roughness and sidewall residues[14]. Nevertheless, the recent demonstration of record-high relaxation times of dry-etched qubits[12] indicates that these problems can be mitigated. Dry etch processes also provide better junction dimension control and reproducibility, making it the preferred technique in state-of-the-art CMOS processing[30].

To characterize fabrication performance, resistances of test Josephson junction arrays with different junction areas are measured at room-temperature. Arrays consist of either 30 or 60 individual test junctions and junction areas range between 0.03 and 0.125 μm^2, as determined from SEM images. The optimized fabrication process results in 99.8% junction yield for 3k dry etch

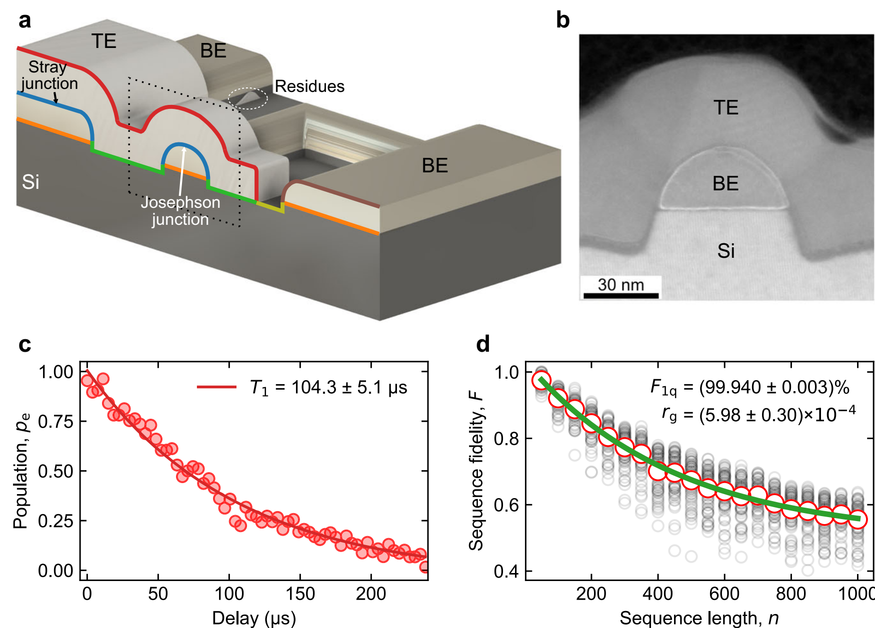

Fig. 1 Overlap junction overview and transmon qubit performance. a Cross-sectional illustration. The overlap between the bottom electrode (BE) and top electrode (TE) defines the Josephson junction and the (parasitic) stray junction. Sidewall residues can be present due to subtractive etching steps, which is discussed later. Si–BE, Si–TE, and junction interfaces are indicated in orange, green, and blue, respectively. The BE–air, TE–air, and Si–air top-surface interfaces are depicted in brown, red, and yellow, respectively. **b** High-angle annular dark-field-scanning tunneling electron microscope (HAADF-STEM) image of a wet-etched BE junction cross-section indicated by the dotted line in **a**. Ar milling induced amorphous Si layer is visible below the TE layer (green interface in **a**). **c** Qubit energy relaxation measurement with $T_1 = 104.3 \pm 5.1$ μs. **d** Average gate fidelity (99.940 ± 0.003)% and average error per gate $(5.98 \pm 0.30) \times 10^{-4}$ measured with randomized benchmarking. The errors of the reported values in **c** and **d** represent the respective standard deviations.

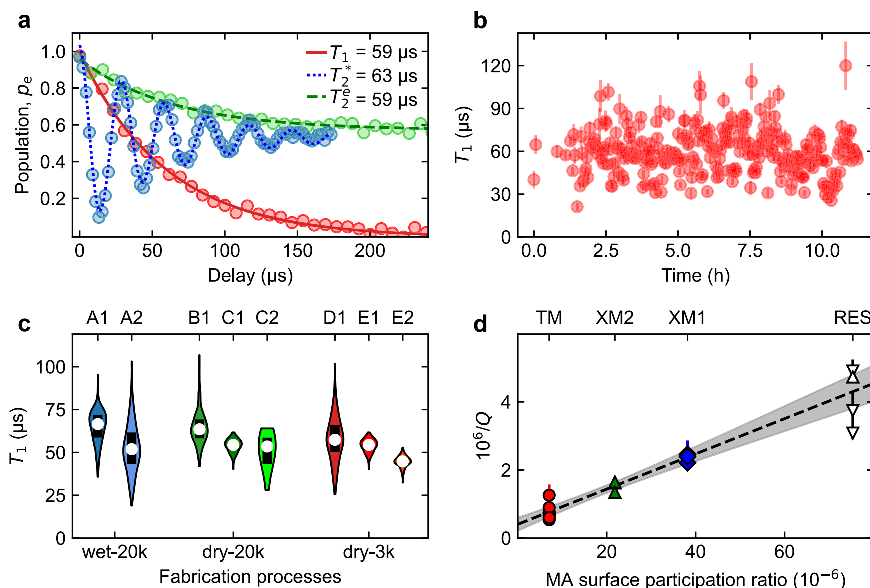

Fig. 2 Qubit coherence time characterization. a Qubit population (device C1) during typical decay time measurements. Line fits are shown for the qubit's lifetime $T_1 = 59.6 \pm 1.4$ μs, and coherence times $T_2^* = 63.8 \pm 3.9$ μs (Ramsey) and $T_2^e = 59.3 \pm 2.0$ μs (spin-echo). **b** Fluctuation of the qubit's energy relaxation time for a period of 11 h (device D1). Error bars represent the T_1 SD from the line fit. **c** Qubit T_1-statistics for several transmon devices, grouped for different process variations. Device names are shown on top. A violin plot is used to visualize the distributions and white dots indicate the mean value. Black bars mark the first and third quartile. Within the measurement uncertainty, no conclusive difference between etch processes and wafers resistivities is observed. **d** Inverse device quality factors (data is corrected for Purcell decay) as a function of MA surface participation ratio. Device types are shown on top. The gray area represents the 95% confidence bounds of the fit to the qubit data. Markers denote the mean *Q*-factor for each device. Error bars indicate the population's SD (or the fit's SD in case of single measurements). Upward and downward empty triangles depict wet and dry-etched RES devices, respectively. RES data reaffirms that both etch processes result in comparable device performance. Device details are presented in Supplementary Table 1.

samples. The resistance's relative standard deviations (RSD) range between 2–5% (Supplementary Fig. 2), which is comparable to the state-of-the-art double-angle evaporated Josephson junctions[23–25,44]. The reported RSD is notably lower than the RSD estimated for previously reported overlap junctions[33]. Based on RSD analysis[24], we conclude that the junction parameter variation is dominated by the variation in junction area (Supplementary Fig. 2).

Overlap Josephson junction qubit performance

High-coherence overlap junction qubits are characterized at 10 mK in a conventional dilution-refrigerator setup (see Methods Section and Supplementary Fig. 3). Double-pad transmon qubits (TM) show typical $T_1 = 59$ μs, Ramsey decoherence time of $T_2^* = 63$ μs and spin-echo decoherence time of $T_2^e = 59$ μs (Fig. 2a). We extract a mean of $T_1 = 58$ μs, with observed values reaching up to 100 μs, from repeated measurements over a span of 11 h for a dry-etched TM qubit fabricated on a 3k Si substrate (Figs. 1c and 2b). The notable T_1 variation has been previously attributed to the presence of fluctuating TLS defects[45,46] and quasiparticle tunneling through the Josephson junction[47] (Supplementary Fig. 6). We note that our reported record values surpass previously reported relaxation times for overlap junction qubits[33,36,38].

The impact of etching processes and substrate resistances on the qubit lifetimes is studied next. We collect T_1 statistics from devices fabricated with different process combinations: wet etch on 20k wafers (wet-20k), dry etch on 20k wafers (dry-20k) and dry etch on 3k wafers (dry-3k). The transmon qubits consistently achieve average T_1 lifetimes between 50–70 μs. The violin plot (Fig. 2c) represents kernel distribution estimates from measured T_1 times for each device. We observe no significant difference between the etch processes and wafer resistivities. This agrees with SEM images, where no visual difference is observed between junctions fabricated by the wet and dry etch processes (Supplementary Fig. 4). The T_1 independence on the substrate resistivity also agrees with our estimation of negligible microwave losses from similar 3k substrates ($Q_i \sim 8$ M) of previous resonator measurements[48], setting an upper limit of the qubit $T_1 > 400$ μs at 3 GHz. Within the measurement uncertainty, the qubit lifetimes, therefore, appear not to be compromised by the dry etch manufacturable process on 3k wafer substrates.

To further investigate the sources of loss in overlap junction qubits, we design and fabricate two additional Xmon type qubits[49] (XM1, XM2) with reduced gaps between the center electrode pad and the ground plane (Supplementary Fig. 5). By engineering the geometry and gap size, we control the participation ratios (fraction of the device's total electric field energy stored in the volume of lossy dielectric materials) of surface interfaces such as the substrate–air (SA) and metal–air (MA) interface[49–51]. For each design, we estimate participation ratios with electrostatic simulations (see Methods section and Supplementary Fig. 5). The Josephson junction's dimensions (Supplementary Table 1), and its associated interface participation ratios are similar and uncorrelated with the qubit design. This allows us to distinguish between losses originating from the junction and its vicinity (junction losses) and from the qubit capacitor pads (capacitor losses).

For a proper comparison of qubit lifetimes of devices at different transition frequencies, *Q*-factors, calculated from mean qubit relaxation times (corrected for Purcell decay[52]) and their transition frequency ($Q = 2\pi T_1 f$)[46,53,54], are compared to the MA participation ratio of different qubit designs. The MA participation ratio was chosen since its interface was found to dominate microwave loss[51] and generally scales with other interface participation ratios (Supplementary Table 2). We find that the reciprocal of the qubit's *Q*-factors (the qubit's total loss) scales with the qubit MA participation ratio, as indicated by the linear fit of the qubit data in Fig. 2d. The linear fit agrees with the on-chip

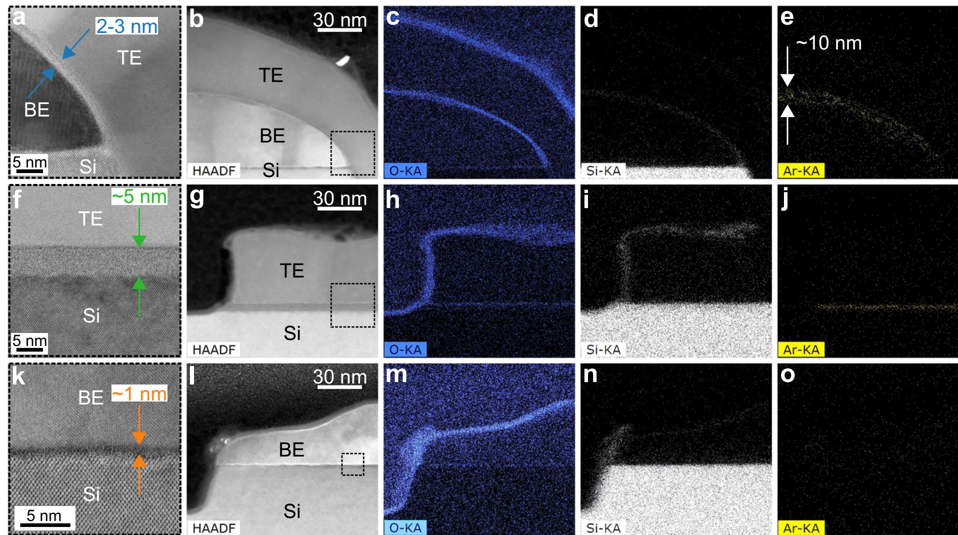

Fig. 3 EDS results of the O/Si/Ar content for dry-etched sample interfaces. For each row, the position of the high-resolution annular bright-field-scanning transmission electron microscope (ABF-STEM) image in the first column is indicated by the dashed square in the HAADF-STEM image in the second column. The four rightmost columns have the same scale. **a**–**e** Josephson junction profile. In addition to O, traces of Ar and Si atoms are found in the junction, likely due to Ar milling during native oxide removal. **f**–**j** Si–TE, TE–air, and Si–air interfaces. The amorphous Si layer (containing Ar and O similar to the junction) is encapsulated below the TE. A Si-rich crust is observed. **k**–**o** Si–BE, BE–air, and Si–air interfaces. Si–BE interface has barely detectable O content. Residues of the Si-rich crust are visible at the BE sidewall, similarly to the TE.

coplanar waveguide resonator (RES) datapoints (open symbols in Fig. 2d). This confirms that qubits and resonators share a common dominant loss source, associated with surface interfaces. For qubits, the dominant loss, therefore, originates from the interfaces at capacitor pads.

From the *y*-axis intercept of the linear fit, we can extract a hypothetical residual loss of $1/Q = (0.41 \pm 0.17) \times 10^{-6}$, corresponding to a postulated, junction-limited $T_1 \approx 131^{+115}_{-41} \mu s$ for a qubit transition frequency of 3 GHz. The uncertainty is estimated from the 95% confidence bound of $1/Q$. The residual loss is associated with the junction and constitutes a combination of losses coming from the Josephson junction and interfaces at its vicinity[41,52,55], the stray junction[56], or quasiparticle tunneling[47]. While quasiparticle tunneling signatures have been observed in T_1 measurements (Supplementary Fig. 6), we cannot quantitatively determine separate contributions from the listed loss sources to the T_1 limit.

Interface characterization

We attempt to correlate the origin of the qubit losses and the possible effect of Ar milling by examining interface morphology and atomic compositions with high-resolution cross-sectional transmission electron microscopy (TEM) and energy-dispersive X-ray spectroscopy (EDS), respectively. The characterization results depicted in Fig. 3 are of a dry-etched qubit device (see Methods section for details).

The fabricated Josephson junction barriers have a typical thickness of 2–3 nm (Fig. 3a), as is also commonly observed for angle-evaporated junctions[57]. No structural damage is seen on top of the BE due to Ar milling (Fig. 3a, b). However, traces of Ar can be detected at the barrier, which extends ~10 nm into the BE (Fig. 3e). Similarly, Si atom traces can be found at the barrier, likely originating from the resputtered Si during the Ar milling (Fig. 3d). An atomic concentration of less than 4% for both elements is observed inside the junction (Supplementary Fig. 7). Impurities can lead to two-level system (TLS) defect losses in the junction[55,56,58]. In our experiment however, they cannot be distinguished from other residual junction losses. High-resolution TEM images of overlap junctions fabricated with dry and wet etch processes show no discernible difference (Supplementary Fig. 4).

At the Si–TE interface, an amorphous Si layer of ~5 nm is visible (Fig. 1a: green interface, Fig. 3f). This is caused by Ar milling, which has been shown to damage the Si substrate[41]. This is also in agreement with traces of Ar found in this layer (Fig. 3j). Damaged Si layer has been reported to host TLS defects, which lead to microwave losses[41]. At the Si–air interface however, no amorphous Si layer can be observed (Fig. 1a: yellow interface, Fig. 3g, l) and no Ar can be detected (Fig. 3j, o). We conclude that the amorphous Si is consumed by the TE etch, except below the TE. The potentially lossy amorphous Si layer constitutes only a small fraction of the total qubit footprint (Supplementary Fig. 5) and likely contributes to the residual junction losses. Near the TE sidewalls, we observed crust residues (Fig. 3g and Supplementary Fig. 4) that consist of oxygen (O) (Fig. 3h) and Si atoms (Fig. 3i). This crust arises from Si deposition on the sidewall and top of the resist during subtractive dry etching[59] (Fig. 1a: red interface). Similar to the amorphous Si layer, this crust can lead to residual microwave losses, however, only in the area surrounding the TE.

A less than 1 nm thin substrate–BE interface layer (Fig. 1a: orange interface, Fig. 3k) shows barely detectable traces of O impurities (Fig. 3m). This indicates that the substrate surface passivation with HF prior to the BE metal deposition successfully prevents oxide growth. The BE shows a distinct metal–air interface profile (Fig. 1a: brown interface), which we attribute to a combination of Ar milling, TE etching and residual BE crusts in case of BE dry etching. Residues of the BE crust and TE Al may be found at the sidewalls due to the anisotropic nature of the Ar milling and TE dry etch (Fig. 3l–n). The absence of Ar signal on the BE–air interface (Fig. 3o) indicates that the TE etch removes the amorphized layer from both the BE–air and Si–air interface.

DISCUSSION

As shown above, qubit devices are limited by the losses associated with the qubit capacitor pads. These losses can originate from crust residues, Al sidewall residues, and native oxides near the BE structures. Since coherence times of wet and dry-etched qubits do

Published in partnership with The University of New South Wales

not significantly differ (Fig. 2c), we can exclude the BE crust remnants from the dominant loss sources. Other contributions cannot be confidently separated at this stage. However, advanced surface treatment steps can be devised to reduce its effects in future implementations.

Residual losses associated with the Josephson junction encompass loss from (i) quasiparticle tunneling, (ii) the stray junction, (iii) crusts and native oxides in the vicinity of the junction, (iv) the amorphous Si interface underneath the TE, and (v) the junction barrier. Quasiparticle tunneling losses can be alleviated by proper filtering of infrared[60] and high-energy radiation[61] or including quasiparticle trapping sites on chip[62]. Stray junction loss can be avoided by using a bandage process to ensure a proper galvanic contact between the TE and capacitor pad[15,24,41,63]. Similarly, as discussed for capacitor losses, crust and native oxides in the vicinity of the junction could be further reduced by developing dedicated surface cleaning processes. On the other hand, the amorphous Si and junction impurities are loss sources specific to Ar milling and can therefore not be easily eliminated. The effect of amorphous Si below the TE could be reduced by minimizing the TE surface area. Potential losses from junction contaminations can only be alleviated by further optimizing the Ar milling step. However, within our measurement uncertainty, their effect currently cannot be distinguished from other losses. To further investigate the junction losses, different qubit designs, such as 3D transmons[50], merged-element transmons[55], or finMETs[31] could be explored.

We have fabricated and measured record-high coherence times for qubits based on overlap junctions, with mean T_1 values comparable to qubits fabricated with double-angle evaporated junctions. We demonstrated a qubit fabrication process that is fully compatible with CMOS fabrication requirements and tools. By studying different qubit designs, we infer that qubit limiting losses are located at the capacitor surface interfaces and that our overlap junctions are not limiting the qubit relaxation times up to at least 131^{+115}_{-41} μs. Further advancements in qubit lifetimes could be achieved by developing specialized surface treatments. The presented qubit fabrication process paves the way for reproducible and well-controlled qubit integration in 300 mm wafer fabrication facilities, expediting the upscaling of quantum computers and other superconducting Josephson junction devices.

METHODS

Overlap Josephson junction fabrication process

The substrate coupons (3 × 3 cm) for the qubit fabrication process are diced from two types of intrinsic Si wafers: 300 mm Si wafer with resistivity 3000 Ω.cm and 100 mm Si wafer with resistivity >20,000 Ω.cm labeled 3k and 20k, respectively. After a close coupled wet etch of the native Si oxide with hydrofluoric acid, a 70 nm of Al (bottom electrode—BE layer) is deposited by magnetron rf sputtering (Pfeiffer Spider 630) at a rate of 0.5 nm/s. Exposure of cleaned silicon surface to air did not exceed 2 min. No atomic impurities from the Ar processing gas could be detected in the EDS measurement of Al films (Fig. 3e, j, o). A 300 mm industry-grade e-beam tool is used to define structures in the PMMA positive resist layer (PMMA AR-P 630–670). The pattern is transferred to the BE layer either by dry or wet etch. For the room-temperature wet etch process we use OPD5262 etchant based on 2% TMAH. Dry etching is done with inductively coupled plasma (ICP) using a $SiCl_4$/He chemistry (Oxford PlasmaLabSystem100). The dry etch process also forms a shallow recess into the Si substrate. During dry etching in the presence of PMMA resist, a Si-rich sidewall crust forms on the BE and resist layer sidewalls. A post-etch residue remover EKC265 is used to simultaneously reduce the presence of resist and minimize sidewall crusts. After resist strip, the native Al oxide on top of the BE is removed by a coupon-wide Ar milling step in the load lock of the sputtering system. Ar milling at rf powers of 100 W yields an Al etch rate of ~1 nm/min. The duration of the Ar mill step is determined as the time needed to obtain a short contact between the TE and BE in a standard JJ fabrication flow without the controlled oxidation step. The Josephson junction (JJ) barrier layer is formed by controlled dynamic oxidation at constant pressure. Without vacuum break, 50 nm of Al is deposited to form the top electrode. The subsequent TE is patterned using dry etching. Process steps for the TE patterning are similar to those for the BE patterning with the exception of using a negative resist (ma-N 2400 series) to minimize the e-beam writing time. The full process flow is visualized in Supplementary Fig. 1. A list of all fabricated samples in this study is found in Supplementary Table 1.

Material characterization

TEM, STEM, and EDS measurements were performed at the Materials Characterization and Analysis center at the IMEC microelectronics research institute. Before characterization, the samples were coated with a spin-on carbon (SOC) layer. Lamellae with a thickness of <50 nm were cut with a focused ion beam (FIB) using Helios 450. TEM, STEM, and EDS measurements were performed on Titan Cubed Themis 300 STEM with a 200 kV source. For this study, TEM, EDS, atomic-resolution HAADF-STEM, and ABF-STEM were used to investigate interfaces between the substrate-top electrode, substrate-bottom electrode, and AlO_x barrier between the top and bottom Al electrodes.

Qubit measurement setup

Overlap qubits are measured with a standard dilution-refrigerator setup (Supplementary Fig. 3). Input lines are thermalized with 20 dB attenuators at three different temperature stages. High-frequency noise above the measurement frequency range is filtered before reaching the qubit with a low-pass filter (VLF-8400 +) with cutoff frequency of 8.4 GHz. Each superconducting qubit chip is placed and wire bonded to the non-magnetic gold-plated copper PCB enclosed in an O-free copper sample holder. The sample holder is thermalized to the mixing chamber plate in a dilution refrigerator. The sample holder is surrounded by the copper radiation shield as well as two cryo-perm shields to minimize magnetic fields at the sample. Output signal lines are thermalized with three isolators (LNF-ISC4_8A) with a total reverse isolation of ~60 dB and a 4–8 GHz band-pass filter (KBF-4/8-2S). The signal is amplified with a HEMT amplifier (LNF-LNC4_8C) at the 4 K stage and ultra-low noise amplifier (LNA-30-04000800-07-10P) at room temperature.

At room temperature, pulsed signals are generated and acquired using the Keysight Quantum Engineering Toolbox: M3202A AWGs and M3102A Digitizer. The qubit excitation and readout pulse are combined at room-temperature and applied to the qubit's feedline. No dedicated charge line or flux line were used to excite or bias qubits.

Three qubit designs were used in this study, two Xmon (XM1, XM2)[49] styles and a two-pad transmon (TM)[14] qubit. Qubit frequencies were targeted in the range of 3–4 GHz and readout resonator frequencies are in the range of 5–6 GHz. Qubit anharmonicities are between 200 and 250 MHz.

Numerical simulations of the participation ratios

The electric field losses are dependent on and are proportional to the participation ratios of the dielectric regions in the devices. The participation ratio p_i in a dielectric i is defined as the fraction of electrical energy contained in the dielectric with respect to the total electrical energy in the device, as follows[64]:

$$p_i = \frac{\epsilon_i \int_{V_i} |E_V|^2 dV}{\sum_i \epsilon_i \int_{V_i} |E_V|^2 dV} \tag{1}$$

where $\in_i$ and V_i correspond to the dielectric constant and volume of the ith dielectric, respectively, and $|E_V|$ correspond to the absolute value of the electric field in the dielectric in an incremental volume dV. To calculate the participation ratio's p_i, we first estimate the electric fields by solving the Poisson's equation in the devices using a commercial TCAD electrostatic simulator[65], and then subsequently incorporate the fields into Eq. (1). We invoke the following approximations for calculating the electric fields in TCAD. First, we omit the Josephson junction region in the electrostatic model, as we are primarily interested in the losses in the capacitor region of the superconducting qubits. Second, with the geometry of the capacitor being largely symmetric along certain axes (see Supplementary Fig. 5a), we perform a two-dimensional electrostatic simulation, rather than a full 3-dimensional calculation. This further offers the advantage of reduced computational time and larger numerical accuracies for the simulations with an extremely refined mesh at interfaces in the device. Third, we only

consider metal–air (MA) and substrate–air (SA) oxide interfaces in the simulations, while omitting the metal-substrate (MS) oxide interface. This is also reasonable considering that there is no substantial oxide formation between the metal and substrate, as indicated in Fig. 3c, m. Furthermore, uncertain parameters are the exact thickness of the oxide at the different interfaces and their dielectric constant. From TEM images, we estimate an average thickness of the SA and MA interfaces of 4 and 5 nm, respectively. The geometry of the structures used in the simulations is very similar to that of the experimental devices, and we also employ commonly chosen values for the dielectric constants, i.e., 11.9, 3.9, and 5.0 for the silicon substrate, silicon dioxide, and metal–air oxide interfaces, respectively.

Based on the above technique, approximations, and parameters, we estimate the participation ratios in the capacitor regions for the different designs (resonator, Xmons, and transmon), which are shown in Supplementary Table 2. These obtained participation ratios have further been used to illustrate the scaling trend of $1/Q$ for the four devices in Fig. 2d. The linear scaling with the participation ratio calculations in Fig. 2d indeed confirms that the major limiting region for the qubit or resonator lifetimes (T_1) is the capacitor.

Randomized benchmarking: measurement and analysis

The average physical gate error r_g and gate fidelity F_{1q} have been measured for device C2 (Fig. 1d). A random sequence of Clifford gates of varying lengths n is applied to a qubit initialized in the ground state. At the end of the sequence, an inverting gate is added to create an overall identity operation and the final qubit state is measured to determine the fidelity. The measurement is repeated 80 times for each sequence length. Cosine pulses with a duration of 50 ns are used in the experiment. The averaged sequence fidelity is fitted to $F = Ap^n + B$, where the parameters A and B depend on the state preparation and measurement errors[42]. From p, we determine r_g as the error per Clifford r_{Clifford} normalized by the average number of physical Clifford generator gates (1.875):

$$r_g = \frac{r_{\text{Clifford}}}{1.875} = \frac{(1-p)(d-1)}{1.875d} \tag{2}$$

where $d = 2^m$ is the dimensionality of the Hilbert space, which is equal to 2 for a single qubit. The average physical gate fidelity is obtained from:

$$F_{1q} = 1 - r_g \tag{3}$$

The coherence limit on the measured fidelity ($F_{1q,\text{inc}}$) is estimated with qubit parameters: $T_1 = 50\ \mu s$ and $T_2^* = 60\ \mu s$[66].

DATA AVAILABILITY

The data are available upon reasonable request.

CODE AVAILABILITY

The codes are available upon reasonable request.

Received: 9 March 2022; Accepted: 18 July 2022;
Published online: 09 August 2022

REFERENCES

1. Kjaergaard, M. et al. Superconducting qubits: current state of play. *Annu. Rev. Condens. Matter Phys.* **11**, 369–395 (2020).
2. Barends, R. et al. Superconducting quantum circuits at the surface code threshold for fault tolerance. *Nature* **508**, 500–503 (2014).
3. Sheldon, S. et al. Characterizing errors on qubit operations via iterative randomized benchmarking. *Phys. Rev. A* **93**, 012301 (2016).
4. Rol, M. A. et al. Restless tuneup of high-fidelity qubit gates. *Phys. Rev. Appl.* **7**, 041001 (2017).
5. Kjaergaard, M. et al. Programming a quantum computer with quantum instructions. Preprint at http://arxiv.org/abs/2001.08838 (2020).
6. Barends, R. et al. Digitized adiabatic quantum computing with a superconducting circuit. *Nature* **534**, 222–226 (2016).
7. Ma, R. et al. A dissipatively stabilized Mott insulator of photons. *Nature* **566**, 51–57 (2019).
8. Kandala, A. et al. Hardware-efficient variational quantum eigensolver for small molecules and quantum magnets. *Nature* **549**, 242–246 (2017).
9. Havlíček, V. et al. Supervised learning with quantum-enhanced feature spaces. *Nature* **567**, 209–212 (2019).
10. Arute, F. et al. Quantum supremacy using a programmable superconducting processor. *Nature* **574**, 505–510 (2019).
11. Wu, Y. et al. Strong quantum computational advantage using a superconducting quantum processor. *Phys. Rev. Lett.* **127**, 180501 (2021).
12. Wang, C. et al. Towards practical quantum computers: transmon qubit with a lifetime approaching 0.5 milliseconds. *NPJ Quantum Inf.* **8**, 1–6 (2022).
13. Somoroff, A. et al. Millisecond coherence in a superconducting qubit. Preprint at http://arxiv.org/abs/2103.08578 (2021).
14. Place, A. P. M. et al. New material platform for superconducting transmon qubits with coherence times exceeding 0.3 milliseconds. *Nat. Commun.* **12**, 1779 (2021).
15. Nersisyan, A. et al. Manufacturing low dissipation superconducting quantum processors. in *2019 IEEE International Electron Devices Meeting (IEDM) 31.1.1-31.1.4*. https://doi.org/10.1109/IEDM19573.2019.8993458 (2019).
16. Chow, J. M., Dial, O. & Gambetta, J. M. IBM Quantum breaks the 100-qubit processor barrier. *IBM Research Blog* https://research.ibm.com/blog/127-qubit-quantum-processor-eagle (2021).
17. Chamberland, C. Topological and subsystem codes on low-degree graphs with flag qubits. *Phys. Rev. X* **10**, 011022 (2020).
18. Yost, D. R. W. et al. Solid-state qubits integrated with superconducting through-silicon vias. *NPJ Quantum Inf.* **6**, 59 (2020).
19. Heinsoo, J. et al. Rapid High-fidelity Multiplexed Readout of Superconducting Qubits. *Phys. Rev. Appl.* **10**, 034040 (2018).
20. Kono, S. et al. Breaking the trade-off between fast control and long lifetime of a superconducting qubit. *Nat. Commun.* **11**, 3683 (2020).
21. Collodo, M. C. et al. Implementation of conditional phase gates based on tunable ZZ interactions. *Phys. Rev. Lett.* **125**, 240502 (2020).
22. Li, X. et al. Tunable coupler for realizing a controlled-phase gate with dynamically decoupled regime in a superconducting circuit. *Phys. Rev. Appl.* **14**, 024070 (2020).
23. Hertzberg, J. B. et al. Laser-annealing Josephson junctions for yielding scaled-up superconducting quantum processors. *NPJ Quantum Inf.* **7**, 129 (2021).
24. Osman, A. et al. Simplified Josephson-junction fabrication process for reproducibly high-performance superconducting qubits. *Appl. Phys. Lett.* **118**, 064002 (2021).
25. Kreikebaum, J. M., O'Brien, K. P., Morvan, A. & Siddiqi, I. Improving wafer-scale Josephson junction resistance variation in superconducting quantum coherent circuits. *Supercond. Sci. Technol.* **33**, 06LT02 (2020).
26. Foroozani, N. et al. Development of transmon qubits solely from optical lithography on 300 mm wafers. *Quantum Sci. Technol.* **4**, 025012 (2019).
27. Dolata, R., Scherer, H., Zorin, A. B. & Niemeyer, J. Single electron transistors with NbÕAlOx ÕNb junctions. *J. Vac. Sci. Technol. B* **21**, 7 (2003).
28. Tsioutsios, I. et al. Free-standing silicon shadow masks for transmon qubit fabrication. *AIP Adv.* **10**, 065120 (2020).
29. Quintana, C. M. et al. Characterization and reduction of microfabrication-induced decoherence in superconducting quantum circuits. *Appl. Phys. Lett.* **105**, 062601 (2014).
30. Wan, D. et al. Fabrication and room temperature characterization of trilayer junctions for the development of superconducting qubits on 300 mm wafers. *Jpn. J. Appl. Phys.* **60**, SBBI04 (2021).
31. Goswami, A. et al. Towards merged-element transmons using silicon fins: the FinMET. Preprint at https://doi.org/10.48550/arXiv.2108.11519 (2022).
32. Kim, S. et al. Enhanced coherence of all-nitride superconducting qubits epitaxially grown on silicon substrate. *Commun. Mater.* **2**, 1–7 (2021).
33. Stehli, A. et al. Coherent superconducting qubits from a subtractive junction fabrication process. *Appl. Phys. Lett.* **117**, 124005 (2020).
34. Bal, M. et al. Overlap junctions for superconducting quantum electronics and amplifiers. *Appl. Phys. Lett.* **118**, 112601 (2021).
35. Winkel, P. et al. Nondegenerate Parametric Amplifiers Based on Dispersion-Engineered Josephson-Junction Arrays. *Phys. Rev. Appl.* **13**, 024015 (2020).
36. Long, J. et al. A universal quantum gate set for transmon qubits with strong ZZ interactions. Preprint at https://doi.org/10.48550/arXiv.2103.12305 (2021).
37. Steffen, M. et al. State tomography of capacitively shunted phase qubits with high fidelity. *Phys. Rev. Lett.* **97**, 050502 (2006).
38. Wu, X. et al. Overlap junctions for high coherence superconducting qubits. *Appl. Phys. Lett.* **111**, 032602 (2017).
39. Wisbey, D. S. et al. Effect of metal/substrate interfaces on radio-frequency loss in superconducting coplanar waveguides. *J. Appl. Phys.* **108**, 093918 (2010).
40. Megrant, A. et al. Planar superconducting resonators with internal quality factors above one million. *Appl. Phys. Lett.* **100**, 113510 (2012).
41. Dunsworth, A. et al. Characterization and reduction of capacitive loss induced by sub-micron Josephson junction fabrication in superconducting qubits. *Appl. Phys. Lett.* **111**, 022601 (2017).
42. Magesan, E., Gambetta, J. M. & Emerson, J. Characterizing quantum gates via randomized benchmarking. *Phys. Rev. A* **85**, 042311 (2012).

43. Richardson, C. J. K. et al. Fabrication artifacts and parallel loss channels in metamorphic epitaxial aluminum superconducting resonators. *Supercond. Sci. Technol.* **29**, 064003 (2016).
44. Pop, I. M. et al. Fabrication of stable and reproducible submicron tunnel junctions. *J. Vac. Sci. Technol. B* **30**, 010607 (2012).
45. Klimov, P. V. et al. Fluctuations of energy-relaxation times in superconducting qubits. *Phys. Rev. Lett.* **121**, 090502 (2018).
46. Burnett, J. J. et al. Decoherence benchmarking of superconducting qubits. *NPJ Quant. Inform.* **5**, 54 (2019).
47. Yan, F. et al. The flux qubit revisited to enhance coherence and reproducibility. *Nat. Commun.* **7**, 12964 (2016).
48. Verjauw, J. et al. Investigation of microwave loss induced by oxide regrowth in high- *Q* niobium resonators. *Phys. Rev. Appl.* **16**, 014018 (2021).
49. Barends, R. et al. Coherent Josephson qubit suitable for scalable quantum integrated circuits. *Phys. Rev. Lett.* **111**, 080502 (2013).
50. Wang, C. et al. Surface participation and dielectric loss in superconducting qubits. *Appl. Phys. Lett.* **107**, 162601 (2015).
51. Melville, A. et al. Comparison of dielectric loss in titanium nitride and aluminum superconducting resonators. *Appl. Phys. Lett.* **117**, 124004 (2020).
52. Deng, H. et al. Titanium nitride film on sapphire substrate with low dielectric loss for superconducting qubits. Preprint at http://arxiv.org/abs/2205.03528 (2022).
53. Gambetta, J. M. et al. Investigating surface loss effects in superconducting transmon qubits. *IEEE Trans. Appl. Supercond.* **27**, 1–5 (2017).
54. Dial, O. et al. Bulk and surface loss in superconducting transmon qubits. *Supercond. Sci. Technol.* **29**, 044001 (2016).
55. Mamin, H. J. et al. Merged-element transmons: design and qubit performance. *Phys. Rev. Appl.* **16**, 024023 (2021).
56. Lisenfeld, J. et al. Electric field spectroscopy of material defects in transmon qubits. *NPJ Quantum Inf.* **5**, 1–6 (2019).
57. Mueller, C., Cole, J. H. & Lisenfeld, J. Towards understanding two-level-systems in amorphous solids: insights from quantum circuits. *Rep. Prog. Phys.* **82**, 124501 (2019).
58. Gordon, L., Abu-Farsakh, H., Janotti, A. & Van de Walle, C. G. Hydrogen bonds in Al2O3 as dissipative two-level systems in superconducting qubits. *Sci. Rep.* **4**, 7590 (2014).
59. Kim, D. W., Jung, M. Y., Choi, S. S., Kim, J. W. & Boo, J. H. The effect of SiCl4 additive gas on the Cl-based Al plasma etch procedure. *Thin Solid Films* **475**, 81–85 (2005).
60. Barends, R. et al. Minimizing quasiparticle generation from stray infrared light in superconducting quantum circuits. *Appl. Phys. Lett.* **99**, 113507 (2011).
61. Cardani, L. et al. Reducing the impact of radioactivity on quantum circuits in a deep-underground facility. *Nat. Commun.* **12**, 2733 (2021).
62. Riwar, R.-P. et al. Normal-metal quasiparticle traps for superconducting qubits. *Phys. Rev. B* **94**, 104516 (2016).
63. Bilmes, A., Händel, A. K., Volosheniuk, S., Ustinov, A. V. & Lisenfeld, J. In-situ bandaged Josephson junctions for superconducting quantum processors. *Supercond. Sci. Technol.* **34**, 125011 (2021).
64. Woods, W. et al. Determining interface dielectric losses in superconducting coplanar-waveguide resonators. *Phys. Rev. Appl.* **12**, 014012 (2019).
65. Synopsys. Sentaurus Device—Technology Computer Aided Design (TCAD) | Synopsys. https://www.synopsys.com/silicon/tcad/device-simulation/sentaurus-device.html (2022).
66. Kosen, S. et al. Building blocks of a flip-chip integrated superconducting quantum processor. *Quantum Sci. Technol.* **7**, 035018 (2022).

ACKNOWLEDGEMENTS

The authors gratefully thank Kristiaan De Greve and Jonas Bylander for their comments after critical reading of the manuscript. The authors also gratefully thank Paola Favia, Hugo Bender, and Chris Drijbooms for metrology support. This work was supported in part by the imec Industrial Affiliation Program on Quantum Computing.

AUTHOR CONTRIBUTIONS

J.V. and A.P. planned the experiment. A.P. designed the samples. Ts.I., J.J. and D.L.P. preformed the sample fabrication, with contributions from D.W. Qubit data was collected by J.V., R.A. and A.M.V. and analyzed by J.V. J.V.D. performed the resonator measurements. A.P. performed the randomized benchmarking and supervised the qubit characterization. Ts.I. performed the room-temperature physical and electrical characterization. F.A.M. performed the participation ratio simulations. J.V. and A.P prepared the manuscript, with input from all authors. M.H, M.M., I.R., B.G. and A.P. supervised and coordinated the project.

COMPETING INTERESTS

The authors declare no competing interests.

ADDITIONAL INFORMATION

Supplementary information The online version contains supplementary material available at https://doi.org/10.1038/s41534-022-00600-9.

Correspondence and requests for materials should be addressed to A. Potočnik.

Reprints and permission information is available at http://www.nature.com/reprints

Publisher's note Springer Nature remains neutral with regard to jurisdictional claims in published maps and institutional affiliations.

Open Access This article is licensed under a Creative Commons Attribution 4.0 International License, which permits use, sharing, adaptation, distribution and reproduction in any medium or format, as long as you give appropriate credit to the original author(s) and the source, provide a link to the Creative Commons license, and indicate if changes were made. The images or other third party material in this article are included in the article's Creative Commons license, unless indicated otherwise in a credit line to the material. If material is not included in the article's Creative Commons license and your intended use is not permitted by statutory regulation or exceeds the permitted use, you will need to obtain permission directly from the copyright holder. To view a copy of this license, visit http://creativecommons.org/licenses/by/4.0/.

© The Author(s) 2022